JOURNAL OF EXPERIMENTAL AND THEORETICAL PHYSICS, 2024, Vol. 166, No. 2(8), pp. 181–194

ATOMS, MOLECULES, OPTICS

SIMULATION OF ENERGY ABSORPTION PROCESSES IN WATER NEAR THE SURFACE OF GOLD NANOPARTICLE UNDER X-RAY PHOTON IRRADIATION

© 2024 A. P. Chaynikov*, A. G. Kochur, A. I. Dudenko

Rostov State Transport University 344038, Rostov-on-Don, Russia
**e-mail: chaynikov.a.p@gmail.com*

Received April 04, 2024,
Revised April 10, 2024
Accepted April 12, 2024

Abstract. Monte Carlo method was used to simulate secondary ionization processes and energy absorption in water around gold nanoparticles with diameters ranging from 2 to 100 nm after photoionization by photons with energies in the range of 20 to 80 keV. The spectra of secondary photons and electrons emitted by nanoparticles arising from cascade decay of inner vacancies in ionized gold atoms were calculated. The average energies re-emitted by nanoparticles by secondary photons and electrons were calculated as functions of nanoparticle diameter, as well as radial dependencies of local absorbed dose in water near the surface of nanoparticles of various diameters. It is shown that the nanoparticle re-emits most of the energy of absorbed primary photons with photoelectrons and Auger electrons. The greatest contribution to the number of secondary ionization events and absorbed dose near the nanoparticle surface comes from Auger electrons formed as a result of cascade relaxation of vacancies in the inner electron shells of gold atoms.

DOI: 10.31857/S004445102408e054

1. INTRODUCTION

Currently, radiosensitizers based on metallic nanoparticles (NPs) are being intensively studied in photon therapy of oncological diseases [1–3]. Delivery of nanoparticles directly to tumor tissue followed by hard X-ray irradiation allows to significantly increase the absorbed dose inside the tumor and minimize radiation damage to healthy tissues.

The physical basis of the effect of radiosensitizers based on metal nanoparticles with high atomic numbers is as follows. First, due to the fact that the photoionization cross-section increases with atomic number, the introduction of nanoparticles containing heavy atoms into the tumor leads to an increased probability of photon absorption within the tumor. Second, during photoionization of nanoparticle atoms by hard ray radiation, the inner shells of nanoparticle atoms are predominantly ionized, and the decay of vacancies in them is a cascade of sequential radiative and non-radiative transitions. As shown in studies [4–6] using the example of vacancy decay in K- and L-shells of Fe, Ag and Au atoms, a significant number of Auger electrons with energies from 10 eV to 15 keV are emitted, which, together with the photoelectron, carry away most of the energy of the initially absorbed photon. Third, the inelastic mean free path of Auger electrons in water and biological tissues ranges from 1 to 10 nm. As a result, Auger electrons emitted by an ionized nanoparticle possess high stopping power and can produce numerous secondary ionization events in the immediate vicinity of the nanoparticle surface within the cancer cell causing radiolysis of water molecules and formation of reactive oxygen species leading to oxidative stress and cancer cell death.

When developing radiosensitizers based on nanoparticles, it is necessary to have quantitative information about the energy spectra of photons and electrons emitted by them, about the number and spatial distribution of secondary ionization events they cause and the energy absorbed in these events, as well as to know the dependence of these characteristics on the composition and size of nanoparticles and on the energy of primary photons. Since experimental determination of these characteristics on a nanometer scale inside the cell is hardly possible, the traditional approach to solving this problem is computer simulation

using the Monte Carlo method. A good review on the application of the Monte Carlo method for modeling radiosensitization processes using metallic nanoparticles is given in [7].

Currently, there are well-established and comprehensively tested software packages for Monte Carlo simulation of ionizing radiation interaction with matter, such as Geant4-DNA [8, 9] and PENELOPE [10]. However, it should be noted that the cascade decay processes of inner-shell vacancies, which play a major role in the radiosensitization mechanism, are described rather crudely in these software packages. The key characteristics in describing the cascade relaxation of electron vacancies in atoms are the partial widths and energies of radiative and non-radiative transitions. Geant4-DNA and PENELOPE use partial widths and transition energies from the EADL library [11], which presents data for transitions from electronic configurations with a single vacancy. At the same time, the cascade decay of a deep vacancy in a heavy atom can consist of a large number of non-radiative transitions. For example, as a result of the decay of a $2s$ -vacancy in a Au^+ ion an average of 9.2 electrons are emitted [12]. Thus, many cascade transitions during the decay of inner vacancies occur in multi-hole electronic configurations. As shown in [13–15], using transition energies from single-hole configurations to describe cascade decays of deep vacancies leads to erroneous accounting of energetically forbidden non-radiative transitions, significant distortion of decay trees, and, consequently, substantial errors in the calculated characteristics of vacancy cascade decays.

On the other hand, there are currently well-developed methods for describing vacancy cascade decays in isolated atoms (see [13] and References therein). In [16, 17], a method was developed for describing vacancy cascade decay processes by construction and analysis of the decay tree. In this method, the transition energy is calculated as the difference between the average total energies of the initial and final multi-hole configurations of the transition, and the possible overlap of multiplets of initial and final configurations is taken into account using the method of global characteristics of atomic spectra [18]. Additionally, in [16, 17], a simple and sufficiently accurate method was proposed for accounting for the influence of electronic configuration on partial transition widths.

The method of constructing and analyzing the decay tree was applied in [6, 12, 13, 19] to describe the decay of vacancies in the inner shells of an isolated gold atom. In [12, 13], the charge spectra of final gold ions formed as a result of cascade decays of inner vacancies in various subshells were calculated. In [6, 19], the spectra of photons and electrons emitted during the cascade relaxation of vacancies were calculated, the average energies re-emitted by the gold atom with photons and electrons were determined, and the dependencies of re-emitted energies on the primary photon energy ionizing the gold atom were calculated in the range from 0.01 to 10^3 keV.

The approximations proposed in [16, 17] for calculating energies and partial transition widths in describing the cascade decay of vacancies were subsequently implemented in the Monte Carlo algorithm for simulating the effects of ionizing radiation on matter [20–23].

In [22], Monte Carlo method was used to calculate the spectra of photons and electrons emitted by isolated iron nanoparticles with diameters from 2 to 130 nm upon absorption of photons with energies up to 11 keV. The energies absorbed by the nanoparticle and re-emitted into the surrounding medium with secondary photons and electrons were determined. It was established that when the energy of primary photons is below the ionization threshold of the K-shell of Fe atom, most of the absorbed photon energy is re-emitted by the nanoparticle with secondary electrons (primarily photo- and Auger electrons) with energy sufficient for ionization of water molecules. When the energy of primary photons is above the K-threshold, a significant portion of energy is carried away from the nanoparticle by $2p - 1s$-photon, emitted with high probability at the first step of $1s$-vacancy decay in the iron atom. With increasing nanoparticle diameter, the number of low-energy electrons emitted with energies up to 10 eV increases. They are formed in secondary ionization events by electron impact of iron atoms inside the nanoparticle. Such low-energy electrons are not capable of ionizing tissue molecules surrounding the nanoparticle but can lead to DNA molecule destruction through the mechanism of dissociative electron attachment [24].

In [23], Monte Carlo simulating of energy dissipation in water during cascade decays of inner-shell vacancies in iron ion Fe^+ located in water was performed. The dependencies of absorbed dose on the distance from iron ion were calculated. It was established that the decay of a single Fe$1s$-vacancy induces on average 232 acts of secondary ionization of water molecules by electron impact, in which approximately 3274 eV is absorbed, and 18 acts of secondary photoionization, in which 256 eV is absorbed.

In this work, the Monte Carlo method implemented in [20–23] is applied to study energy

absorption processes occurring in water near the surface of a gold nanoparticle irradiated with photons having energies from 20 to 80 keV. The aim of this work is to calculate the radial distribution of secondary ionization events and absorbed dose depending on the energy of primary photons and nanoparticle diameter.

2. METHOD OF CALCULATION

Simulation of photon and electron interaction processes with atoms is perfomed in a spherical interaction zone with a radius of $R_{zone} = 100$ μm, which is approximately 10 times larger than the characteristic linear size of cancer cells. At the center of the interaction zone, there is a gold nanoparticle with a diameter D_{NP} ranging from 2 to 100 nm, and the space outside the nanoparticle is filled with water (Fig. 1). The nanoparticle and water are considered in the approximation of non-interacting atoms. The volume concentration of gold atoms in the nanoparticle equals $n_{\mathrm{Au}} = 5.90 \cdot 10^{22}$ cm^{-3} corresponding to the density of solid gold 19.3 g/cm^3. The concentrations of oxygen and hydrogen atoms in water, $n_{\mathrm{O}} = 3.34 \cdot 10^{22}$ cm^{-3} and $n_{\mathrm{H}} = 2n_{\mathrm{O}}$, correspond to liquid water with a density of 1 g/cm^3.

Each Monte Carlo test begins with photoionization of one of the nanoparticle atoms by a photon with energy $h\nu$. The location of initial photoionization is randomly selected assuming equal probability of photon absorption at any point inside the nanoparticle, since the mean free path of incident photons is many times larger than the NP diameter. The selection of the ionized nl_j-subshell of the gold atom is performed using a random number generator based on partial photoionization cross sections. As a result of primary photoionization, a photoelectron is produced, which is added to the list of secondary electrons for further simulation of its track in the interaction zone, and a vacancy is created in the nl_j-subshell of the ionized atom. Then, the procedure for simulating the cascade decay of the formed vacancy is initiated.

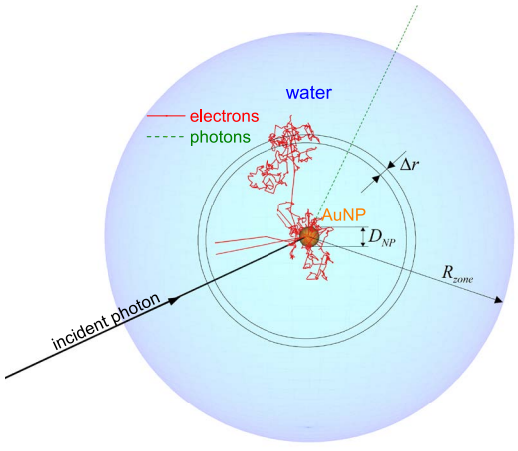

Fig. 1. Scheme illustrating the Monte Carlo experiment. Black solid line – primary photon incident on the nanoparticle, red solid lines – tracks of secondary electrons, green dashed lines – secondary photons

2.1. Simulating of vacancy cascade decay

Let $C^{(0)}$ be the initial electronic configuration of an ionized gold atom with a vacancy in the nl_j-subshell. At the first decay step, all energetically and symmetrically allowed radiative and non-radiative (Auger, Coster-Kronig, and super-Coster-Kronig) transitions from configuration $C^{(0)}$ to configurations $C^{(1)}$ are analyzed. For each allowed transition $C^{(0)} \to C_\alpha^{(1)}$, partial widths $\Gamma(C^{(0)} \to C_\alpha^{(1)})$ are calculated and relative probabilities $\chi(C^{(0)} \to C_\alpha^{(1)})$, also called branching ratios, are determined:

$$\chi(C^{(0)} \to C_\alpha^{(1)}) = \frac{\Gamma(C^{(0)} \to C_\alpha^{(1)})}{\sum\limits_{\alpha'} \Gamma(C^{(0)} \to C_{\alpha'}^{(1)})}. \qquad (1)$$

After that using a random number generator based on the calculated branching ratios (1), one of the possible transitions $C^{(0)} \to C_\alpha^{(1)}$ is selected, and the photon (in case of radiative transition) or electron (in case of non-radiative transition) emitted as a result of the selected transition is added to the list of secondary photons and electrons for further tracking of their propagation.

If the configuration $C_\alpha^{(1)}$ formed as a result of the first decay step has vacancies in inner subshells, the cascade decay modeling continues. Transitions filling each of the inner vacancies present in configuration $C_\alpha^{(1)}$ are analyzed, and partial widths and branching ratios are calculated for all allowed transitions. Then, based on the calculated branching ratios, one of the transitions $C_\alpha^{(1)} \to C_\beta^{(2)}$ is randomly selected, and the photon or electron emitted as a result of the transition is added to the list of analyzed secondary particles.

The modeling of vacancy cascade decay continues until a transition is selected after another step that leads to the formation of a stable ionic configuration where all vacancies are located in the outermost subshell.

The energies of cascade transitions are calculated as the differences between the average energies

of the initial and final ionic configurations of the transition, pre-calculated in the Pauli-Fock approximation [25, 26], taking into account spin-orbital splitting. The multiplet structure of levels caused by electrostatic interaction of electrons is approximately accounted by using the method of global characteristics of atomic spectra [18]. In the case of closely-lying-in-energy configurations, to account for multiplet overlap, the energy and partial width of the transition are adjusted, as described in detail in [13]. In total, to model the cascade decays of vacancies in the gold atom, it was necessary to optimize 86,592 different multi-hole ionic configurations.

To calculate the partial widths of radiative and non-radiative transitions, the radial parts of atomic orbitals calculated in the Pauli-Fock approximation are used. The approximation proposed in [16, 17] is used, which allows relatively simple and acceptably accurate calculation of transition widths in arbitrary ionic configurations containing an arbitrary number of vacancies in different subshells. A detailed description of the procedure for calculating partial widths of transitions in arbitrary multi-hole configurations is given in [13, 23]. Also, [13] provides calculated partial widths of radiative and non-radiative transitions in a gold atom with one vacancy.

2.2. Simulating the propagation of secondary photons and electrons

After completing the simulation of the cascade decay of a vacancy in the initially ionized gold atom within the NP, the simulation of secondary photons and electrons propagation begins. The propagation of secondary particles in the interaction zone is considered in the pair collision approximation, within which the interaction of the considered particle with matter represents a set of sequential interaction acts between the particle and individual atoms of the substance [27]. Between two such consecutive acts of interaction (emission, absorption, or scattering), the particle (photon or electron) moves in a straight line. The particle's free path s is generated based on the mean free path λ:

$$s = -\lambda \ln(\xi), \tag{2}$$

where ξ is the value of a random variable with uniform law in the interval $(0;1)$. The mean free path of a particle in matter is calculated based on the interaction cross sections of the considered particle with medium atoms σ_a and atomic concentrations n_a:

$$\lambda = \frac{1}{\sum\limits_a n_a \sigma_a}. \tag{3}$$

If the considered particle is inside the NP, then its mean free path is calculated based on interaction cross sections with Au atom (in the denominator of formula (3) stands $n_{Au}\sigma_{Au}$), and if the particle is in water, then based on interaction cross-sections with atoms H and O (in the denominator stands $n_H\sigma_H + n_O\sigma_O$). If as a result of a random length free path s the particle crosses the NP boundary moving from NP to water or vice versa, then the intersection point of the particle trajectory with the NP surface is determined. Then from this point, a new step is made in the same direction, but with a random length s', calculated based on the particle interaction cross sections with atoms of the area into which the particle had moved.

In this work, we consider the photoionization of a gold NP by photons with energy up to 80 keV, which is less than the ionization potential of gold atom's 1s-shell, $I_{Au1s} \approx 81$ keV. Therefore, the deepest vacancy that can form in an atoms of gold as a result of primary photoionization, is a vacancy in the 2s-subshell, whose ionization potential equals $I_{Au2s} \approx 14.4$ keV. Consequently, the maximum energy of secondary photons formed as a result of vacancy decay in NP atoms does not exceed 14.3 keV. In this energy range, for both gold and water, the photoionization cross section exceeds the coherent and Compton scattering cross sections by 1–3 orders of magnitude. Therefore, when modeling the propagation of secondary photons in the interaction zone, we neglect coherent and Compton scattering and only consider photoionization processes. Thus, a photon emitted during vacancy decay is either absorbed by one of the atoms within the interaction zone (in the NP or in water) or leaves the zone. In the case of photon absorption inside the zone, based on partial photoionization cross sections, using a random number generator, the choice of the ionized atom (O or H for photon absorption in water) and the ionized subshell is made. In the case of inner subshell ionization of Au or O atoms, the above-described procedure for modeling cascade vacancy relaxation is initiated, and the photons and/or electrons emitted during this process are added to the list of secondary particles for further analysis.

The partial cross sections of photoionization for gold, oxygen, and hydrogen atoms used in modeling the propagation of secondary photons were calculated in the dipole approximation using Pauli-Fock wave functions in [6] for Au and [23] for O and H, and are in good agreement with data from other authors. Here we present

the total photoionization cross section of the gold atom (Fig. 2) and the total photoionization cross section of the water molecule (Fig. 3) calculated as the sum of photoionization cross sections of hydrogen and oxygen atoms, $\sigma_{H_2O} = 2\sigma_H + \sigma_O$, in comparison with cross sections from the NIST SRD 126 database [28] for photoionization processes and for coherent and Compton scattering.

When simulating the propagation of secondary electrons, two types of processes are considered: elastic scattering of an electron on an atom and atom ionization by electron impact. The total cross section of electron interaction with an atom a (a = Au,O,H) at electron kinetic energy t consists of the elastic scattering cross section and impact ionization cross section,

$$\sigma_a^{tot}(t) = \sigma_a^{elast}(t) + \sigma_a^{ioniz}(t)$$

The ionization cross section of an atom a by electron impact, in turn, consists of partial ionization cross sections of all its nl-subshells,

$$\sigma_a^{ioniz}(t) = \sum_{nl} \sigma_{a,nl}^{ioniz}(t)$$

If after a free path with a random length calculated using formula (2) with total cross sections $\sigma_a^{tot}(t)$, the electron remains in the interaction zone (in NP or in water), then using a random number generator, an atom with which the electron collided is selected (O or H if the electron experienced a collision in water), and then the type of event that occurred (elastic scattering or ionization of any atomic subshell) is selected.

In case of selecting elastic scattering, using differential with respect to the polar scattering angle v elastic scattering cross sections $d\sigma_a^{elast}(t,v)/dv$ a new direction of electron motion is randomly selected.

In the case of selecting the ionization process of the nl-subshell of atom a by electron impact based on the differential with respect to the energy of the ejected electron ε cross section of ionization of the given subshell $d\sigma_{a,nl}^{ioniz}(t,\varepsilon)/d\varepsilon$ a random selection of energy of the ejected electron ε is performed, and the energy of the scattered electron decreases:

$$t' = t - I_{a,nl} - \varepsilon,$$

where $I_{a,nl}$ is the ionization potential of the nl-subshell of atom a. Further, based on the law of conservation of momentum, the new direction of motion of the scattered electron and the direction of motion of the ejected electron are determined. The vacancy formed as a result of ionization in the nl-subshell of atom a is analyzed for the possibility of its decay, and if the decay is possible, then the procedure for its simulation is initiated.

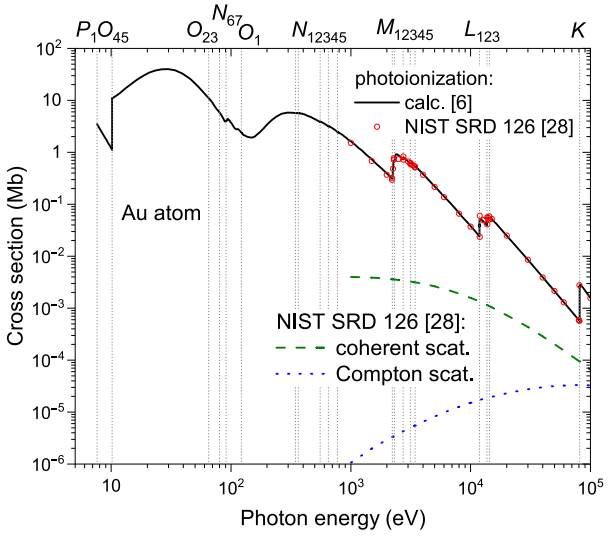

Fig. 2. Cross sections of photon interaction with Au atom. Solid line – total photoionization cross section, calculated in [6] and used in this work. NIST SRD 126 database data [28]: circles – photoionization cross section, dashed line – coherent scattering cross section, dotted line – Compton scattering cross section. Vertical dotted lines mark Au ionization distribution

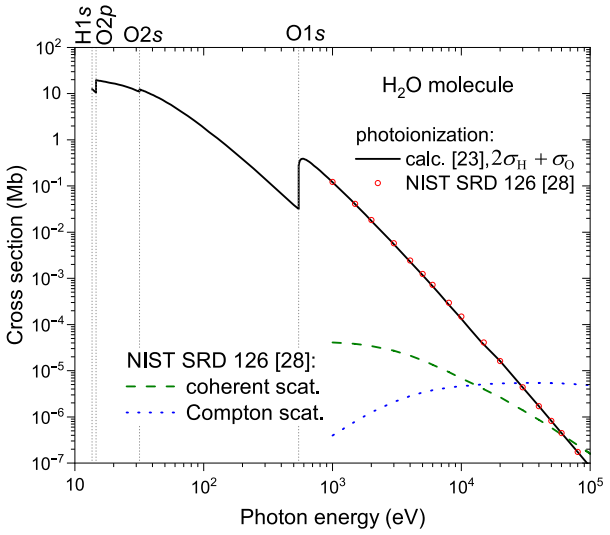

Fig. 3. Photon – water molecule interaction cross-sections. Solid line – total photoionization cross section calculated in [23] as the sum of photoionization cross sections of hydrogen and oxygen atoms and used in this work. NIST SRD 126 database data [28]: circles – photoionization cross section, dashed line – coherent scattering cross section, dotted line – Compton scattering cross section. Vertical dotted lines mark the ionization thresholds of O and H

Differential $d\sigma_a^{elast}(t,v)/dv$ and total $\sigma_a^{elast}(t)$ cross sections of elastic electron scattering on atoms Au, O and H at electron energy $t < 50$ eV were calculated in the partial wave approximation [29] using the radial parts of the scattered electron wave functions calculated in the Pauli–Fock approximation. At electron energy $t > 50$ eV, elastic scattering cross sections from the NIST SRD 64 electronic database [30] are used in the simulations.

The ionization cross sections of atoms Au, O and H by electron impact during the simulation were calculated using the semi-empirical binary-encounter Bethe (BEB) approximation [31]. For electron energies above 10 keV, a relativistic modification of the BEB approximation was used [32]. The partial and total ionization cross sections of atoms by electron impact calculated in this approximation are presented in Fig. 4 for Au atom and in Fig. 5 for atoms H and O in comparison with theoretical and experimental results of other authors [31, 33–36]. Also, Fig. 5 shows the electron impact ionization cross section of the water molecule, calculated in the independent atom approximation as the sum of ionization cross sections of individual H and O atoms, $\sigma_{H_2O}^{ioniz} = 2\sigma_H^{ioniz} + \sigma_O^{ioniz}$. As can be seen, the impact ionization cross section of the H_2O molecule obtained in this way is in good agreement with the calculation results of Hwang et al. [37], where the BEB approximation [31] was used to calculate the ionization cross sections of molecular orbitals of molecule H_2O, and with the experimental data of Bolorizadeh and Rudd [38].

Fig. 6 shows the mean free paths of photons in solid gold and liquid water. The solid lines represent the mean free paths calculated considering only photoionization processes using the photoionization cross sections of atoms Au, O and H used in the simulations. The circles in Fig. 6 show the mean free paths of photons obtained from mass attenuation coefficients from the NIST SRD 8 database [39] taking into account both photoionization processes and coherent and Compton scattering of photons. A slight difference between our results and data [39] is observed for water (Fig. 6*b*) at photon energies above 15 keV, which is due to our neglect of Compton scattering. However, as noted above, since secondary photons with energies above 14.3 keV are not generated during simulations, this cannot significantly affect the simulation results.

Fig. 7 shows the dependencies of the mean inelastic (due to impact ionization processes) electron free path in solid gold and liquid water on electron energy, using ionization cross sections of atoms Au, O and H by electron impact in the BEB approximation, which are used in the simulation of the propagation of secondary electrons. For both water and gold, good agreement with results from other authors [40–47] is observed.

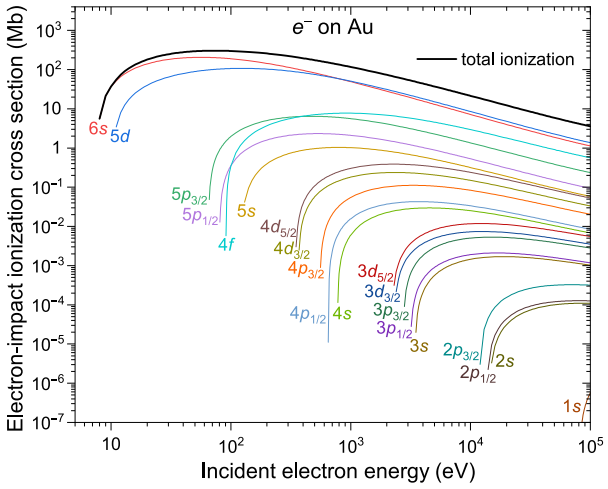

Fig. 4. Partial and total cross sections of Au atom ionization by electron impact, calculated in the binary-encounter Bethe approximation

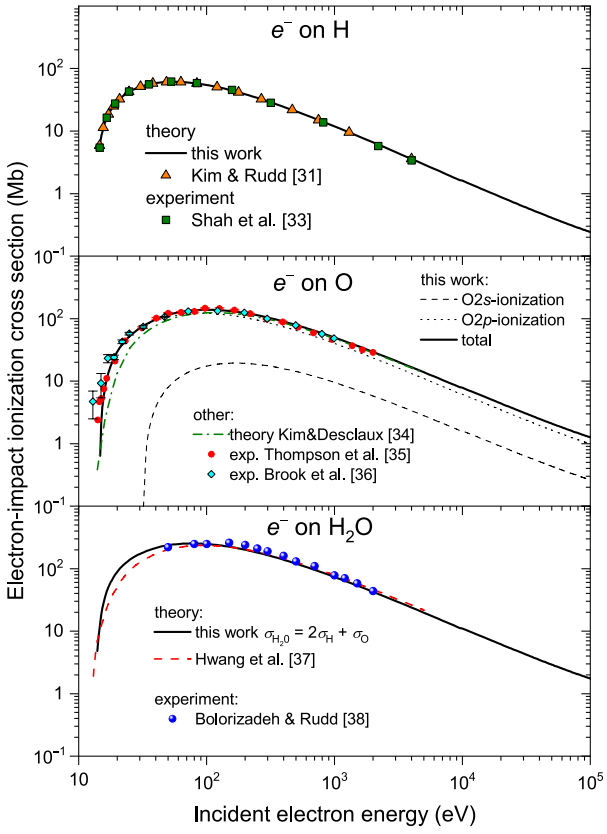

Fig. 5. Electron impact ionization cross sections for H atom (upper panel), O atom (middle panel), and water molecule (lower panel)

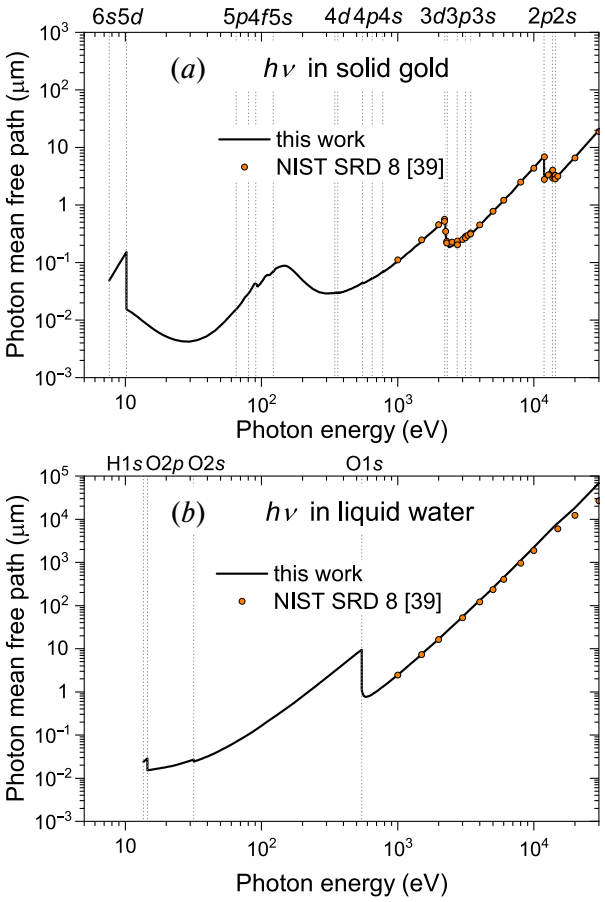

Fig. 6. Mean free paths of photons in solid gold (*a*) and in liquid water (*b*). Solid lines are calculations based on photoionization cross sections of atoms Au, O, and H [23], which are used in this work. Circles represent calculations based on mass attenuation coefficients from NIST SRD 8 database [39] accounting for coherent and Compton scattering

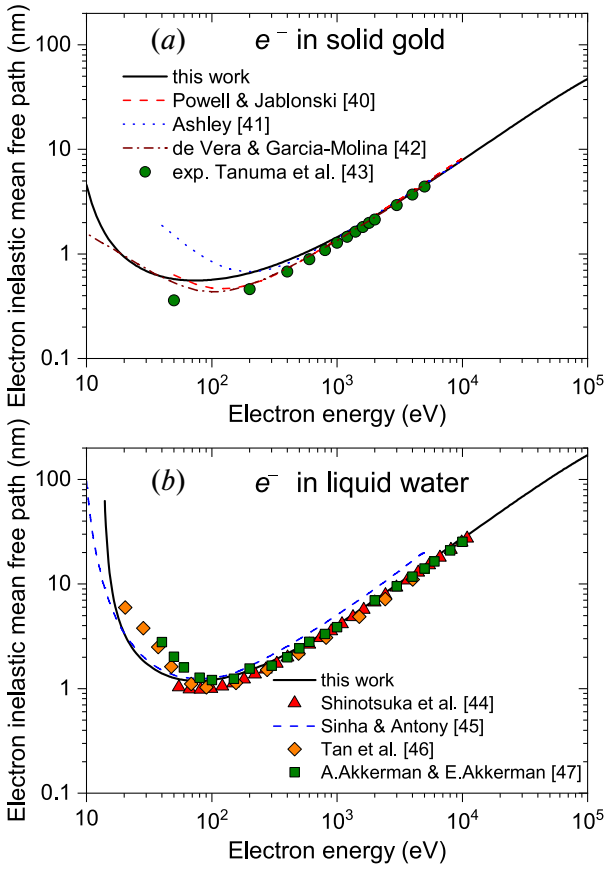

Fig. 7. Mean inelastic electron free paths in solid gold (*a*) and in liquid water (*b*)

The simulation of secondary electron propagation within the interaction zone during a single Monte Carlo test continues until each electron either leaves the zone, or until its energy becomes insufficient for ionization of H and O atoms (the minimum threshold energy for electrons equals the ionization potential of the hydrogen atom $I_{\mathrm{H}1s} = 13.6$ eV). After running a large number of tests (in this work, each Monte Carlo experiment consisted of 10^5 tests), the calculated characteristics are averaged over all trials, i.e., they represent mean values per one primary photon absorbed by the NP.

2.3. Calculated Characteristics

As a result of the simulation, spectra of photons and electrons emitted by the gold NP into the surrounding aqueous medium are calculated. The energy scale is divided into equal intervals of 10 eV width, for each of which the simulation determines the average number of particles (photons or electrons) with energy within this interval, emitted by the NP as a result of one primary photoionization act.

To study the spatial distribution of secondary ionization acts occurring within the interaction zone and the energy absorbed in these acts, the spherical interaction zone is divided into concentric spherical layers with thickness of $\Delta r = 1$ nm centered at the zone's center and the NP center, see Fig. 1. As a result of the simulation, for each i^{th} sphercal layer bounded by the spheres with radii $r_i - \Delta r/2$ and $r_i + \Delta r/2$, the average number of secondary ionization acts of atoms by electron impact $\Delta N^{el}_{ioniz}(r_i)$ and the average number of secondary photoionization acts $\Delta N^{phot}_{ioniz}(r_i)$ are determined.

In each ionization act, the ionized atom absorbs a certain amount of energy. The energy absorbed by the atom as a result of ionization and subsequent decay of the formed vacancy (in case of ionization of one of the atom's inner subshells) is calculated

as the difference between the ionization potential of the ionized subshell and the total energy of all photons and/or electrons emitted during the vacancy decay. During simulation, for each i^{th} spherical layer, the average energies absorbed by atoms in it due to electron impact ionization acts $\Delta E_{abs}^{el}(r_i)$ and photoionization acts $\Delta E_{abs}^{phot}(r_i)$ are determined.

The dependence of the local absorbed dose in water on the distance from the center of NP is calculated as

$$D(r_i) = \frac{\Delta E_{abs}^{el+phot}(r_i)}{\rho \Delta V(r_i)}, \quad (4)$$

where

$$\Delta E_{abs}^{el+phot}(r_i) = \Delta E_{abs}^{el}(r_i) + \Delta E_{abs}^{phot}(r_i)$$

is the total energy absorbed inside the i^{th} spherical layer as a result of secondary ionization of atoms by electron impact and secondary photoionization, $\rho \Delta V(r_i)$ is the mass of the i^{th} spherical layer, ρ is water density, $\Delta V(r_i)$ is the volume of the spherical layer.

Besides $\Delta N_{ioniz}^{el}(r_i)$ and $\Delta N_{ioniz}^{phot}(r_i)$ for individual water layers, the number of secondary water ionization acts by electron impact $N_{ioniz}^{el}(r)$ and the number of secondary photoionization acts $N_{ioniz}^{phot}(r)$ occurring inside a sphere of radius r, and the absorbed energies $E_{abs}^{el}(r)$ and $E_{abs}^{phot}(r)$:

$$\begin{aligned} N_{ioniz}^{el}(r) &= \sum_{R_{NP} < r_i \leqslant r} \Delta N_{ioniz}^{el}(r_i), \\ E_{abs}^{el}(r) &= \sum_{R_{NP} < r_i \leqslant r} \Delta E_{abs}^{el}(r_i), \\ N_{ioniz}^{phot}(r) &= \sum_{R_{NP} < r_i \leqslant r} \Delta N_{ioniz}^{phot}(r_i), \\ E_{abs}^{phot}(r) &= \sum_{R_{NP} < r_i \leqslant r} \Delta E_{abs}^{phot}(r_i), \end{aligned} \quad (5)$$

where R_{NP} is the NP radius.

3. RESULTS AND DISCUSSION

When using gold NPs as radiosensitizers in photon therapy, one of the important questions is choosing the energy of incident photons at which maximum increase in the absorbed dose inside the tumor is achieved. To select the optimal energy of incident photons, as a first approximation, one can use the ratio of mass energy absorption coefficients in water containing gold NPs and in pure water:

$$k(h\nu) = \frac{w_{Au}\mu_{en}^{Au}(h\nu) + (1 - w_{Au})\mu_{en}^{H_2O}(h\nu)}{\mu_{en}^{H_2O}(h\nu)} \quad (6)$$

where $\mu_{en}^{H_2O}$ and μ_{en}^{Au} are mass energy absorption coefficients in water and gold (μ_{en} represents the relative portion of photon energy that transforms into charged particle energy in the process of the interaction of photons and secondary particles with substance atoms in a layer with unit mass per unit area [48]), and w_{Au} is the relative mass fraction of gold in water. Fig. 8 shows the dependence of coefficient k on the energy of incident photons $h\nu$ calculated using mass energy absorption coefficients from NIST SRD 126 database [28], at $w_{Au} = 1\%$. As can be seen, the highest value of absorption enhancement coefficient k is achieved at photon energy ≈ 40 keV and is about 2.6.

Using the method described in section 2, Monte Carlo simulations were performed for processes occurring as a result of absorption of a single 40 keV photon by gold NPs of various diameters (from 2 to 100 nm).

Fig. 9 shows the spectra of secondary electrons and photons emitted by gold nanoparticles with diameters of 2, 20, and 50 nm after absorption of a 40 keV photon. In the electron spectrum (Fig. 9*a*), on the low-energy side of each diagram line corresponding to photo- or Auger electrons, there is a "tail" caused by energy losses of photo- and Auger electrons inside the NP due to secondary inelastic processes. As the NP diameter increases, the average number of inelastic scattering events experienced by photo- and Auger electrons inside the NP

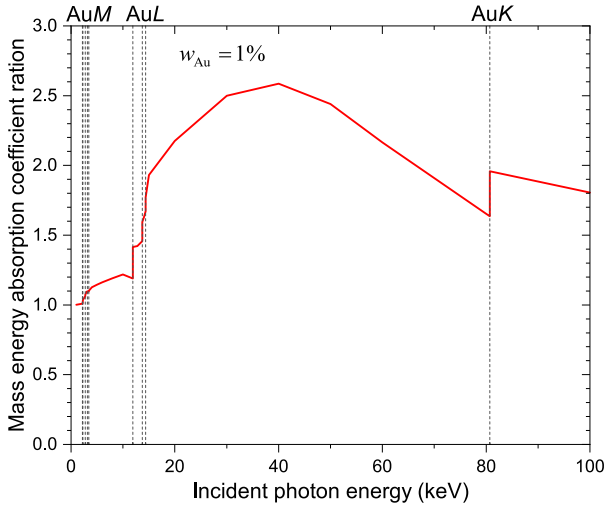

Fig. 8. Dependence of the ratio of mass energy absorption coefficients in water with gold NPs and in pure water (6) on the energy of incident photons at relative mass content of gold 1%

before escaping increases, resulting in decreased intensity of diagram lines and increased area under the continuous "tail" on the low-energy side.

In the photon spectrum (Fig. 9*b*), with increasing NP diameter, a noticeable decrease in intensity is observed only in the low-energy region of the spectrum, from 50 to 200 eV. In this energy region, the mean free path of photons in solid gold (Fig. 6*a*) varies in the range from 9 to 88 nm, therefore the probability of photon absorption of such energy inside a gold NP with a diameter of several tens of nanometers is quite high. In the high-energy region of the spectrum, 8.4–13.8 keV, the mean free path of photons in gold is in the range of 2.9–7.1 μm, which greatly exceeds the NP dimensions. Therefore, the intensity of the photon spectrum in this energy region practically does not depend on the NP diameter.

Table 1 presents the calculated average values of various integral characteristics at primary photon energy of 40 keV depending on the gold NP diameter. With increasing NP diameter from 2 to 100 nm, the energy absorbed by NP increases from 0.64 to 3.16 keV. Most of the absorbed photon energy is re-emitted by NP with electrons whose energy is sufficient to ionize water molecules surrounding the NP. With increasing NP diameter, due to the increase in the number of inelastic electron scattering events inside the NP, there is a decrease in the average number of such electrons from 6.71 at $D_{NP} = 2$ nm to 0.32 at $D_{NP} = 100$ nm and their average total from 35.99 to 32.88 keV respectively. For the same reason, with increasing NP diameter, the number of low-energy electrons (incapable of ionizing water molecules)emitted by the NP increases.

Fig. 10 shows the calculated radial distributions of absorbed dose in water (4) near the surface of gold NPs with diameters of 2, 20, and 50 nm when the NP absorbs one photon with energy of 40 keV. The highest value of local absorbed dose is observed in immediate proximity to the NP surface. With increasing distance from the NP center, the absorbed dose decreases quite rapidly, remaining, however, up to distances of 160–180 nm higher than the typical therapeutic value. With increasing NP diameter, the dose absorbed near its surface decreases, but at distances from the NP center greater than 200 nm, the radial distributions of the absorbed dose for the NPs of different diameters become practically identical. Along with the results of this work, symbols in Fig. 10 show Monte Carlo simulation results [49] using the Geant4-DNA software package [8]. For the NPs with diameters of 20 and 50 nm, our results are in good agreement with [49]. However, for the 2 nm diameter NP at distances from its

Table 1. Average values of various integral characteristics during absorption of a 40 keV photon by gold nanoparticles of different diameters

Calculated value	Nanoparticle diameter, nm				
	2	10	20	50	100
Energy absorbed by NP, keV	0.64	1.00	1.42	2.36	3.16
Number of photons emitted by NP	2.28	2.04	1.77	1.29	0.87
Energy re-emitted by NP with photons, keV	3.32	3.26	3.27	3.24	3.20
Number of electrons emitted by NP with energy sufficient to ionize water molecules	6.71	4.30	2.94	1.23	0.32
Energy re-emitted by NP with electrons capable of ionizing water molecules, keV	35.99	35.56	34.99	33.84	32.88
Number of low-energy electrons emitted by NP with energy insufficient to ionize water molecules	11.4	54.4	102	206	294
Energy re-emitted by NP with low-energy electrons unable to ionize water molecules, keV	0.05	0.18	0.31	0.56	0.76
Energy absorbed in water due to secondary photoionization events, keV	2.15	2.12	2.09	2.02	1.96
Energy absorbed in water due to secondary electron impact ionization events, keV	26.03	25.71	25.30	24.45	23.74
Number of low-energy electrons formed in the interaction zone with energy insufficient to ionize water molecules	2007	2023	2039	2076	2108
Energy of low-energy electrons formed in the interaction zone, keV	8.27	8.30	8.29	8.26	8.23

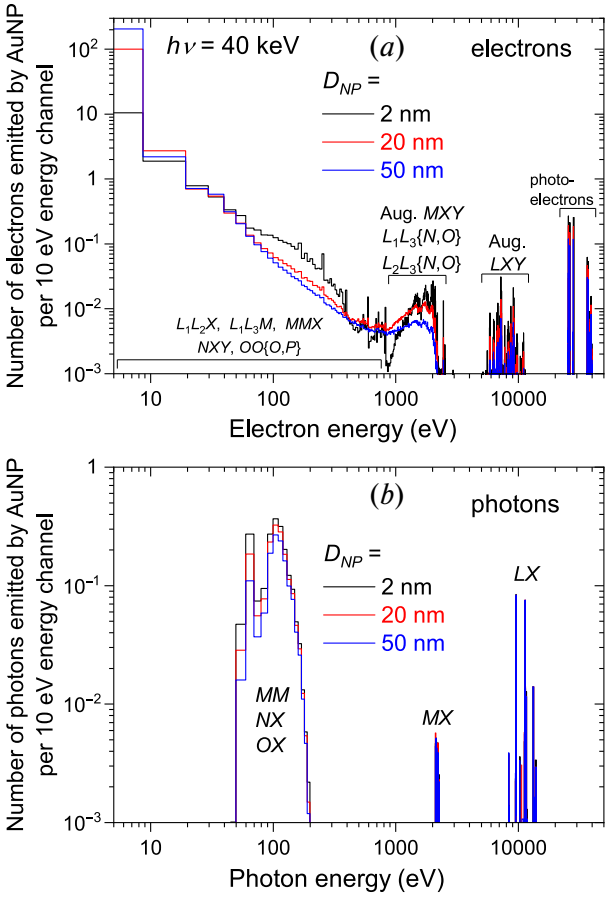

Fig. 9. Calculated spectra of electrons (*a*) and photons (*b*) emitted by gold nanoparticles with diameters of 2, 20, and 50 nm as a result of absorption of a 40 keV photon

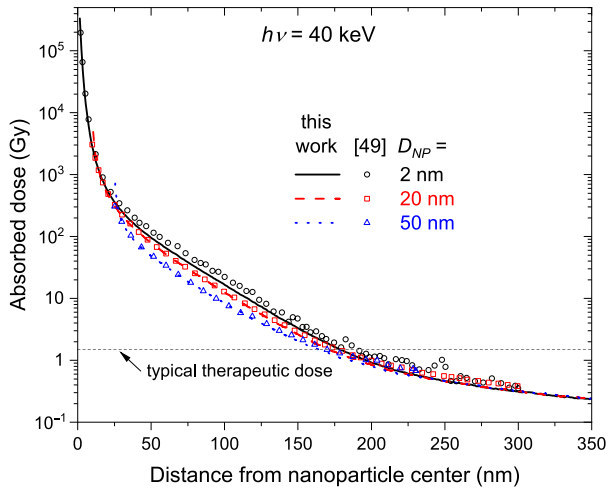

Fig. 10. Dependencies of local absorbed dose in water near the surface of gold NPs with diameters of 2, 20, and 50 nm upon absorption of a 40 keV photon. Lines – calculation of this work, symbols – results of Monte Carlo simulation [49] using Geant4-DNA code

center greater than 20 nm, our calculation results are on average 20% less than those of [49].

From the above results, it follows that with the same mass content of nanoparticles inside tumor tissue, to achieve the highest number of secondary electrons emitted by them which are capable of ionizing water molecules, and the highest value of absorbed dose around the NP, NPs of small sizes should be used.

To investigate the dependence of the characteristics considered above on the energy of primary photons, the simulations were performed for a 10 nm diameter NP at primary photon energies from 20 to 80 keV (between the thresholds of $I_{\mathrm{Au}2s} = 14.4$ keV and $_{\mathrm{Au1}} = 81$ keV).

Fig. 11 shows the number of secondary acts of water molecules ionization by electron impact $N^{el}_{ioniz}(r)$ (Fig. 11*a*) and secondary photoionization $N^{phot}_{ioniz}(r)$ (Fig. 11*b*) depending on the radius of the sphere r within which they occur (5), at different energies of photons ionizing a 10 nm gold NP. With increasing sphere radius r the numbers of secondary ionization acts $N^{el}_{ioniz}(r)$ and $N^{phot}_{ioniz}(r)$ increase, reaching saturation. Table 2 shows the radii of spherical regions R^{el}_{sat} and R^{phot}_{sat}, within which 95% of the maximum number of secondary ionization acts by electron impact and photoionization occur, the numbers of secondary ionization acts in these regions and $N^{phot}_{ioniz}(R^{phot}_{sat})$, as well as the energies absorbed in these $E^{el}_{abs}(R^{el}_{sat})$ and $E^{phot}_{abs}(R^{phot}_{sat})$.

The increase in the number of electron impact ionizations of water molecules $N^{el}_{ioniz}(R^{el}_{sat})$ and the radius R^{el}_{sat} of the region where they occur, with increasing energy of ionizing NP photons, is due to the increase in energy of the photoelectron formed as a result of primary photoionization of one of the NP atoms. In each act of secondary ionization of O and H atoms of water molecules by electron impact, the photoelectron loses only a small portion of its energy. Therefore, with increasing photoelectron energy, the number of secondary ionization events it can produce before its deceleration increases, i.e., until its energy becomes insufficient for water molecule ionization. As a result, and due to the increase in the inelastic mean free path of electrons in water (Fig. 7*b*), the average distance that a photoelectron can travel from the NP before its deceleration increases.

To illustrate this, we performed additional simulation that did not account for the photoelectron formed during primary photoionization of the NP.

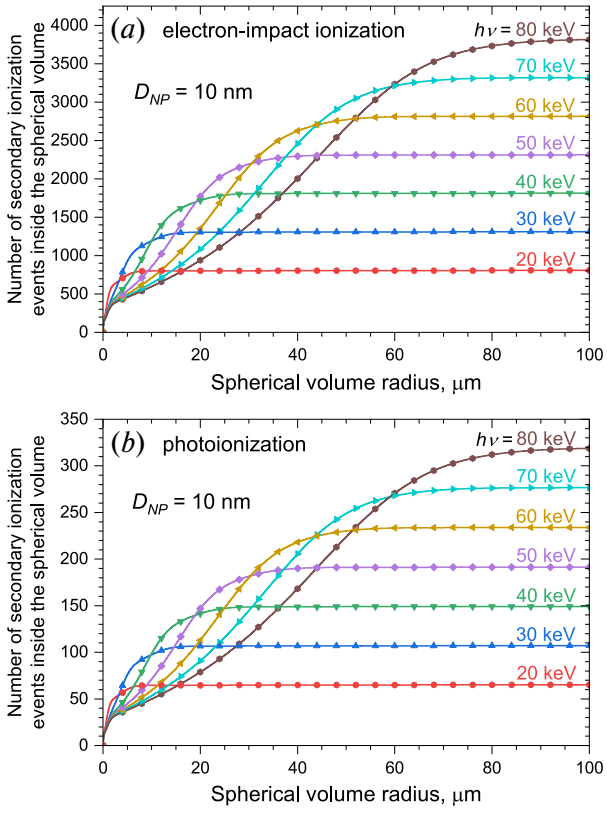

Fig. 11. Dependencies of the number of secondary water ionization events by electron impact (*a*) and the number of secondary photoionization events (*b*) on the radius of the sphere within which they occur, at various energies of the primary photon absorbed by a 10 nm diameter gold NP

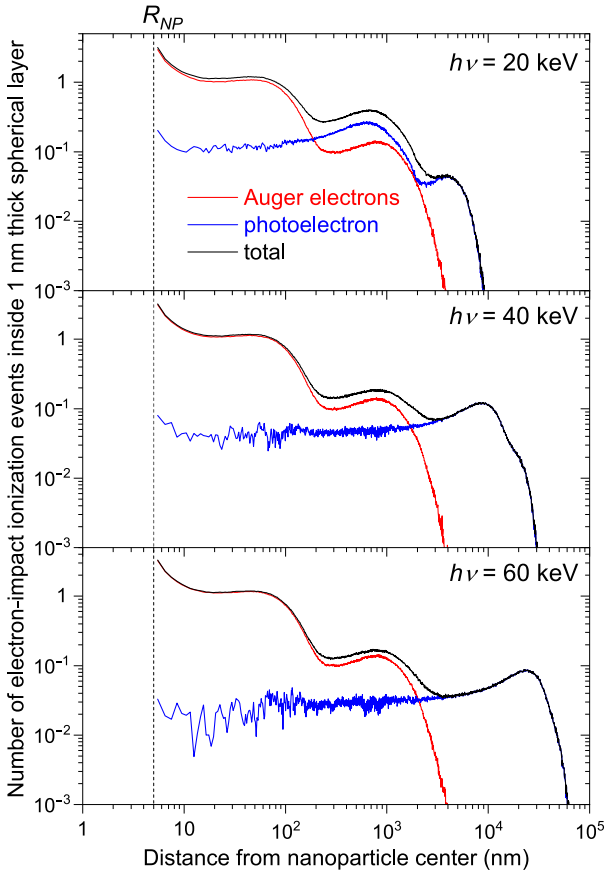

Fig. 12. Numbers of secondary water ionization events by electron impact inside spherical layers with thickness of $\Delta r = 1$ nm depending on the distance from the NP center at different energy of primary photons ionizing a 10 nm diameter gold NP

This allowed separating the contributions of photo- and Auger electrons emitted by the NP to the total number of secondary photoionization events. Fig. 12 shows the dependencies of secondary water ionization events $\Delta N^{el}_{ioniz}(r)$ inside spherical layers with thickness of $\Delta r = 1$ nm induced by photo- and Auger electrons at different energies of primary photons. As can be seen, near the NP surface, the greatest contribution to the number of ionization processes comes from Auger electrons emitted by the NP, while far from the NP – from the photoelectron. Moreover, with increasing energy of primary photons, the distances interval where the photoelectron contribution dominates becomes wider and shifts further from the NP center.

At the energies of primary photons under consideration, $I_{\mathrm{Au}2s} < h\nu < I_{\mathrm{Au}1s}$ the main processes of primary photoionization of NP atoms are the ionization of $2s$-, $2p_{1/2}$- and $2p_{3/2}$-subshells of the Au atom, therefore the Auger electrons emitted by NP are formed mainly as a result of the cascade decays of these initial vacancies. With increasing energy of primary photons in the range from 20 to 80 keV, the relative probability of photoionization of the $2s$-subshell of Au atom increases from 0.18 to 0.38, while the relative probabilities of photoionization of and $2p_{3/2}$-subshells decrease from 0.24 to 0.19 and from 0.34 to 0.20 respectively. As a result, the spectrum of Auger electrons emitted by NP changes, the average number of emitted Auger electrons and their average carried-away energy increases [6]. These changes lead to a relatively small increase in the number of secondary water ionization acts produced by Auger electrons, but, as can be seen in Fig. 12, practically do not affect their spatial distribution.

Regarding the acts of secondary photoionization of water, their main source is not the photons emitted by NP, but secondary photons formed in water as a result of radiative L_1L_{23}-transitions in oxygen atoms ionized by electron impact. The energy of OL_1L_{23}-photon equals 17.2 eV, which is sufficient for ionization

Table 2. Radii of spherical regions R_{sat}^{el} and R_{sat}^{phot}, within which the number of secondary ionization acts by electron impact and the number of secondary photoionization acts reach saturation, numbers of ionization acts $N_{ioniz}^{el}(R_{sat}^{el})$ and $N_{ioniz}^{phot}(R_{sat}^{phot})$ and respective absorbed energies $E_{abs}^{el}(R_{sat}^{el})$ and $E_{abs}^{phot}(R_{sat}^{phot})$ at different primary photon energies $h\nu$, ionizing a 10 nm gold

$h\nu$, keV	R_{sat}^{el}, μm	$N_{ioniz}^{el}(R_{sat}^{el})$	$E_{abs}^{el}(R_{sat}^{el})$, keV	R_{sat}^{phot}, μm	$N_{ioniz}^{phot}(R_{sat}^{phot})$	$E_{abs}^{phot}(R_{sat}^{phot})$, keV
20	5.71	767	10.86	5.70	62	0.88
30	12.00	1245	17.65	11.99	102	1.45
40	20.17	1722	24.42	20.14	142	2.02
50	30.24	2197	31.16	30.18	182	2.59
60	42.36	2674	37.95	42.28	222	3.16
70	56.23	3152	44.73	56.12	263	3.74
80	72.22	3623	51.43	72.10	303	4.31

of the hydrogen atom and 2*p*-subshell of oxygen atom. The mean free path of a photon with such energy in water is approximately 16.6 nm (Fig. 6*b*), therefore it will be absorbed with high probability not far from the atom by which it was emitted, and the number of secondary photoionization acts produced by OL_1L_{23}-photons will be equal to the number of ionization acts of 2*s* -subshell of oxygen atoms by electron impact [23]. In this regard, presented in Fig. 11*b* dependencies of the number of secondary photoionization events $N_{ioniz}^{phot}(r)$ on the radius of the sphere within which they occur practically repeat in shape the corresponding dependencies of the number of secondary ionization events by electron impact $N_{ioniz}^{el}(r)$ for the same primary photon energy values (Fig. 11a). Therefore, the radii of spherical regions R_{sat}^{el} and R_{sat}^{phot} (Table 2) practically coincide, and the ratio of the number of secondary ionization events by electron impact to the number of secondary photoionization events does not depend on the energy of primary photons and equals

$$N_{ioniz}^{el}(R_{sat}^{el})/N_{ioniz}^{phot}(R_{sat}^{phot}) \approx 12.$$

However, it should be noted that in the spectrum of photons emitted by gold NPs (Fig. 9*b*), there are photons emitted as a result of radiative *LX*-transitions during the decay of vacancies in the *L*-shell of initially ionized gold atoms. The average number of these photons per one primary photoionization is about 0.28, and the average energy per photon is 10.7 keV. At this energy, the mean free path of photons in water (Fig. 6*b*) is approximately 2.9 mm, which is significantly larger than the interaction zone radius $R_{zone} = 0.1$ mm, therefore these photons are likely to leave the interaction zone.

Note that the above results are obtained per one primary photon absorbed by the nanoparticle and correspond to processes occurring on the scale of just one or several cells. However, in application to photon therapy, the question of the absorbed dose on a larger scale is also important – the dose absorbed inside the entire tumor, given its size, depth of location, concentration of introduced NPs, and characteristics of the incident X-ray beam. Monte Carlo calculations of this kind were carried out in [50, 51].

4. CONCLUSIONS

The results obtained in this work can be useful in developing methods of photon therapy using gold NPs as radiosensitizers. The presented results indicate that in the case of targeted delivery of NPs directly to cancer cell nuclei, it is more advantageous to use NPs of small diameter to achieve maximum radiation damage near NP surfaces. When choosing the energy of primary photons, along with the traditional requirement of achieving maximum increase in absorbed dose inside the tumor, it is necessary to consider the spatial distribution of secondary ionization acts produced by photoelectrons near the NP surface (Fig. 12). For example, it makes sense to choose the energy of primary photons slightly above the ionization threshold of the L_1-shell of Au atom, so that the regions of ionization damage produced by photo- and Auger electrons coincide.

FUNDING

This study was supported by the Russian Science Foundation (grant No. 22–72-00042), https://rscf.ru/project/22–72-00042/.

REFERENCES

1. Y. Liu, P. Zhang, F. Li, X. Jin, J. Li, W. Chen, and Q. Li, Theranostics **8,** 1824 (2018); https://doi.org/ 10.7150/thno. 22172 .

2. Z. Kuncic and S. Lacombe, Phys. Med. Biol. **63,** 02TR01 (2018); https://doi.org/10.1088/1361-6560/aa99ce.

3. Y. A. Finogenova, A. A. Lipengolts, V. A. Skribitsky, K. E. Shpakova, A. V. Smirnova, A. V. Skribitskaya, N. N. Sycheva, E. Y. Grigorieva, Medical Physics **3,** 70 (2023); https://doi.org/10.52775/1810-200X-2023-99-3-70-86.

4. A. G. Kochur, A. P. Chaynikov, A. I. Dudenko, and V. A. Yavna, J. Quant. Spectrosc. Radiat. Transf. **286,** 108200 (2022); https://doi.org/10.1016/j.jqsrt.2022 . 108200.

5. A. P. Chaynikov, A. G. Kochur, A. I. Dudenko, and V. A. Yavna, J. Quant. Spectrosc. Radiat. Transf. **310,** 108714 (2023); https://doi.org/10.1016/j.jqsrt.2023 . 108714.

6. A. P. Chaynikov, A. G. Kochur, A. I. Dudenko, and V. A. Yavna, J. Quant. Spectrosc. Radiat. Transf. **302,** 108561 (2023); https://doi.org/10.1016/j.jqsrt.2023 . 108561.

7. F. Moradi, K. Rezaee Ebrahim Saraee, S. F. Abdul Sani, and D. A. Bradley, Radiat.Phys. Chem. **180,** 109294 (2021); https://doi.org/10.1016/j.radphyschem.2020.109294.

8. S. Incerti et al., Int. J. Model. Simul. Sci. Comput. **1,** 157 (2010); https://doi.org/10.1142/S179396231000 0122.

9. A. Taheri, M. U. Khandaker, F. Moradi, and D. A. Bradley, Radiat. Phys. Chem. **212,** 111146 (2023); https://doi.org/10.1016/j.radphyschem.2023. 111146.

10. J. M. Fernandez-Varea, G. Gonzalez-Munoz, M. E. Galassi, K. Wiklund, B. K. Lind, A. Ahnesjo, and N. Tilly, Int. J. Radiat. Biol. **88,** 66 (2012); https://doi.org/10.3109/09553 002.2011.598209 .

11. S. T. Perkins, D. E. Cullen, and M. H. Chen, J. Rathkopf, J. Scofield, and J. H. Hubbell, *Tables and Graphs of Atomic Subshell and Relaxation Data Derived from the Llnl Evaluated Atomic Data Library (Eadl)*, Z =1-100, Technical Report UCRL-50400, Vol. 30 (1991).

12. A. P. Chaynikov, A. G. Kochur, A. I. Dudenko, and V. A. Yavna, Opt. Spectrosc. **131,** 529 (2023); http://dx.doi.org/10.61011/EOS.2023.04.56366.456022

13. A. P. Chaynikov, A. G. Kochur, A. I. Dudenko, I. D. Petrov, and V. A. Yavna, Phys. Scr. **98,** 025406 (2023); https://doi.org/10.1088/1402-4896/acb407 .

14. A. P. Chaynikov, A. G. Kochur, A. I. Dudenko, and V. A. Yavna, Phys. Scr. **98,** 095402 (2023); https:// doi.org/10.1088/1402-4896/aceaee .

15. A. P. Chaynikov, A. G. Kochur, and A. I. Dudenko, Phys. Scr. **99,** 045407 (2024); https://doi.org/ 10.1088/1402-4896/ad3157.

16. A. G. Kochur, A. I. Dudenko, V. L. Sukhorukov, and I. D. Petrov, J. Phys. B: At. Mol. Opt. Phys. **27,** 1709 (1994); https://doi.org/10.1088/0953-4075/27/9/011 .

17. A. G. Kochur, V. L. Sukhorukov, A. J. Dudenko, and P. V. Demekhin, J. Phys. B: At. Mol. Opt. Phys. **28,** 387 (1995); https://doi.org/10.1088/0953-4075/28/3/ 010.

18. S. Kucas and R. Karazija, Phys. Scr. **47,** 754 (1993); https://doi.org/10.1088/0031-894 9/47/6/012 .

19. A. P. Chaynikov, A. G. Kochur, A. I. Dudenko, and V. A. Yavna, Phys. Scr. **98,** 095406 (2023); https:// doi.org/10.1088/1402-4896/acef6e .

20. A. G. Kochur, A. P. Chaynikov, and V. A. Yavna, Eur. Phys. J.D **73,** 80 (2019); https://doi.org/10.1140/epjd/e2019-90185-2.

21. A. G. Kochur, A. P. Chaynikov, and V. A. Yavna, J. Electron Spectrosc. Relat. Phenomena **238,** 146863 (2020); https://doi.org/10.1016/j.elspec.2019.05.012

22. A. P. Chaynikov, A. G. Kochur, and V. A. Yavna, Radiat. Eff. Defects Solids **177,** 814 (2022); https://doi.org/10.1080/10420150.2022.2082296 .

23. A. P. Chaynikov, A. G. Kochur, A. I. Dudenko, JETP **164,** 927 (2023); https://doi.org/10.31857/S0044451023120076.

24. I. I. Fabrikant, S. Eden, N. J. Mason, and J. Fedor, Adv. Atom. Mol. Opt. Phys. **66,** 545 (2017); https:// doi.org/10.1016/bs.aamop.2017.02.002 .

25. R. Kau, I. D. Petrov, V. L. Sukhorukov, and H. Hotop, Z.Phys. D Atom., Mol. Clust. **39,** 267 (1997); https://doi.org/10.1007/s004600050137 .

26. V. L. Sukhorukov, I. D. Petrov, B. M. Lagutin, A. Ehresmann, K.-H. Schartner, and H. Schmoranzer, Phys. Rep. **786,** 1 (2019); https://doi.org/10.1016/ j.physrep.2018.10.004.

27. A. F. Akkerman, *Modeling of Charged Particle Trajectories in Matter*, Energoatomizdat, Moscow (1991).

28. J. H. Hubbell and S. M. Seltzer, *X-Ray Mass Attenuation Coefficients, NIST Standard Reference Database* **126,** NIST, PML, Radiation Physics Division (2004); https://dx.doi.org/10.18434/T4D01F .

29. I. I. Sobelman, *Introduction to the Theory of Atomic Spectra*, Nauka, Moscow (1977) [I. I. Sobelman, Introduction to the Theory of Atomic Spectra, Elsevier (1972); https://doi.org/10.1016/C2013-0-02394-8].

30. A. Jablonski, F. Salvat, and C. J. Powell, *NIST Electron Elastic-Scattering Cross- Section Database, Version 3.2,* NIST, Gaithersburg, MD (2010); https://dx.doi.org/10.18434/T4NK50 .

31. Y.-K. Kim and M. E. Rudd, Phys. Rev. A **50,** 3954 (1994); https://doi.org/10.1103/PhysRev A.50.3954 .

32. Y.-K. Kim, J. P. Santos, and F. Parente, Phys. Rev. A **62,** 052710 (2000); https://doi.org/10.1103/PhysRev A.62.052710.

33. M. B. Shah, D. S. Elliott, and H. B. Gilbody, J. Phys. B: At. Mol. Phys. **20,** 3501 (1987); https:// dx.doi.org/10.1088/0022-3700/20/14/022 .

34. Y.-K. Kim and J.-P. Desclaux, Phys. Rev. A **66,** 012708 (2002); https://doi.org/10.1103/PhysRevA . 66.012708.

35. W. R. Thompson, M. B. Shah, and H. B. Gilbody, J. Phys. B: At. Mol. Opt. Phys. **28,** 1321 (1995); https://dx.doi.org/10.1088/0953-4075/28/7/023 .

36. E. Brook, M. F. A. Harrison, and A. C. H. Smith, J. Phys. B: At. Mol. Phys. **11,** 3115 (1978); https:// dx.doi.org/10.1088/0022-3700/11/17/021 .

37. W. Hwang, Y.-K. Kim, and M. E. Rudd, J. Chem. Phys. **104,** 2956 (1996); http://dx.doi.org/10.1063/ 1.471116.

38. M. A. Bolorizadeh and M. E. Rudd, Phys. Rev. A **33,** 882 (1986); https://doi.org/10.1103/PhysRev A.33.882.

39. M. J. Berger, J. H. Hubbell, S. M. Seltzer, J. Chang, J. S. Coursey, R. Sukumar, D. S. Zucker, and K. Olsen, *NIST Standard Reference Database 8 (XGAM)*, NIST, PML, Radiation Physics Division (2010); https://dx.doi.org/10.18434/T48G6X .

40. C. J. Powell and A. Jablonski, J. Phys. Chem. Ref. Data **28,** 19 (1999); https://doi.org/10.1063/ 1.556035 .

41. J. C. Ashley, J. Electron Spectros. Relat. Phenomena **50,** 323 (1990); https://doi.org/10.1016/0368-2048 (90)87075-Y.

42. P. de Vera and R. Garcia-Molina, J. Phys. Chem. C **123,** 2075 (2019); https://doi.org/10.1021/acs.jpcc . 8b10832.

43. S. Tanuma, S. Ichimura, K. Goto, and T. Kimura, J. Surf. Analysis **9,** 285 (2002); https://doi.org/ 10.1384/jsa.9.285.

44. H. Shinotsuka, S. Tanuma, and C. Powell, Surf. Interface Analysis **54,** 534 (2022); https://doi.org/ 10.1002/sia.7064.

45. N. Sinha and B. Antony, J. Phys. Chem. B **125,** 5479 (2021); https://doi.org/10.1021/acs.jpcb.0c10781 .

46. Z. Tan, Y. Xia, M. Zhao, and X. Liu, Radiat. Environ. Biophys. **45,** 135 (2006); https://doi.org/10 . 1007/s00411-006-0049-0.

47. A. Akkerman and E. Akkerman, J. Appl. Phys. **86,** 5809 (1999); https://doi.org/10.1063/1.371597 .

48. J. H. Hubbell, Int. J. Appl. Radiat. Isot. **33,** 1269 (1982); https://doi.org/10.1016/0020-708X(82) 90248-4.

49. S. J. McMahon et al., Sci.Rep. **1,** 18 (2011); https://doi.org/10.1038/srep00018 .

50. I. V. Shchegolkov, I. N. Sheino, V. F. Khokhlov, A. A. Lipengolts, Medical Physics **4,** 12 (2010).

51. I. A. Konobeev, Y. A. Kurachenko, I. N. Sheino, News of Higher Educational Institutions. Nuclear Power Engineering **1,** 155 (2019); https://doi.org/ 10.26583/npe.2019.1.14.